Performance and energy utilization analysis of transcritical CO2 two-phase ejector considering non-equilibrium phase changes

Applied Energy 372 (2024) 123810

Contents lists available at ScienceDirect

Applied Energy

journal homepage: www.elsevier.com/locate/apenergy

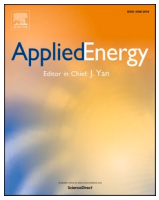

Performance and energy utilization analysis of transcritical CO_2 two-phase ejector considering non-equilibrium phase changes

Hongbing Ding [a], Yuanyuan Dong [a], Yan Yang [b,*], Chuang Wen [c,*]

[a] Tianjin Key Laboratory of Process Measurement and Control, School of Electrical and Information Engineering, Tianjin University, Tianjin 300072, China
[b] Faculty of Environment, Science and Economy, University of Exeter, Exeter EX4 4QF, UK
[c] School of the Built Environment, University of Reading, Reading RG6 6AH, UK

HIGHLIGHTS

- CO_2 two-phase model using phase change for CO_2 ejector in refrigeration systems.
- Two-phase flow behavior and entrainment performance of the ejector are analyzed.
- Exergy destruction and working efficiency under different conditions are calculated.
- The efficiency increases up to 31% while the primary temperature rises to 313.7 K.
- With the back pressure of 4.0 MPa, the exergy destruction ratio is as high as 72.9%.

ARTICLE INFO

Keywords:
Transcritical CO_2 ejector
Two-phase flow
Phase change
Entrainment performance
Energy loss
refrigeration

ABSTRACT

The use of ejectors in transcritical CO_2 refrigeration systems is of key significance for improving system performance, and the investigation of ejectors is particularly important. In this paper, a CO_2 two-phase numerical model considering non-equilibrium phase change is established to investigate the two-phase flow characteristics and entrainment performance in the ejector under different operating conditions. In particular, this study is devoted to the trade-off analysis of internal mass transfer and energy utilization efficiency. After a series of tests, the accuracy of the numerical model has been validated, and with the increase of primary inlet pressure, the entrainment performance first increases and then decreases, while the entrainment performance is greatly improved with the increase of primary temperature. There is a critical back pressure, beyond which the entrainment performance drops rapidly. If the pressure reaches 8.46 MPa and the corresponding temperature is set at 303.7 K, the efficiency of the ejector is 27%. When the temperature rises to 313 K, the efficiency increases to 31%, and the ratio of exergy destruction decreases from 48.3% to 10.2%. However, when the back pressure drops to 4.0 MPa, the working efficiency is only 1.8%, which fails to work normally. Effectively balancing the inlet conditions with energy utilization is a key strategy for optimizing ejector use.

1. Introduction

Global warming and ecological degradation pose a significant threat to the long-term development of human society, making carbon neutrality increasingly important in climate governance. Traditional refrigerants containing fluorine have caused significant damage to the ozone layer and accelerated environmental degradation [1]. The United Nations convened a meeting to sign the Montreal Protocol [2], which directly restricted the use of HCFCs and HFCs refrigerants [3], thereby reducing the potential environmental harm of these traditional greenhouse refrigerants. This demonstrates the determination of governments worldwide to build a low-carbon, environmentally friendly society and also highlights the urgent need to promote green, energy-saving, and low-carbon transitions in the refrigeration industry [4–7].

One of the new and efficient refrigeration technologies, the transcritical CO_2 heat pump [8] using the natural working substance CO_2, has garnered widespread attention. R744, namely CO_2, is classified as a low GWP (near 1) refrigerant [9,10]. Comparing to fluorine-based refrigerants, R744 is safer and more environmentally friendly, avoiding secondary fatal effects due to refrigerant leaks in the system. Additionally, CO_2 is abundant in nature, relatively inexpensive, and exhibits high

* Corresponding authors.
E-mail addresses: y.yang7@exeter.ac.uk (Y. Yang), c.wen@reading.ac.uk (C. Wen).

https://doi.org/10.1016/j.apenergy.2024.123810
Received 11 January 2024; Received in revised form 27 April 2024; Accepted 24 June 2024
Available online 3 July 2024

Nomenclature

E_R	entrainment ratio (−)
m_p	primary mass flow rate, kg/s
m_s	secondary mass flow rate, kg/s
ρ	density, kg m^{-3}
u	velocity, m s^{-1}
p	fluid pressure, Pa
E	total energy, J/kg
k	thermal conductivity, W m^{-1} K^{-1}
h	static enthalpy, J/kg
V_B	volume of the bubble, m^{-3}
k	turbulence kinetic energy, J/kg
Kn	Knudsen number, −
$\dot{m}$	mass change rate, kg m^{-3} s^{-1}
R	bubble radius, m
p_v	threshold pressure, Pa
p	fluid pressure, Pa
C	semi-empirical coefficient, −
c	speed of sound, m s^{-1}
T	temperature, K
$\vec{u}$	velocity vector, m s^{-1}
i,j,k	velocity component, m s^{-1}
n	bubble number density, kg m^{-3}
F_s	safety factor, −

Greek

γ	thermal diffusivity, m^2 s^{-1}
ε	relative error of two meshes, −
ϵ	refinement factor ratio, −
ϑ	CO_2 molecule volume, m^3
κ_B	Boltzmann's constant,
α	volume fraction,
λ	thermal conductivity, W m^{-1} K^{-1}
μ	molecular dynamic viscosity, Pa s
σ	liquid surface tension, N/m

Acronyms

GCI	grid convergence index
MRE	maximum relative error, −
RE	Relative error, −

Subscripts

eff	effective
k	different phase
in, out	inlet, outlet
p	primary
s	secondary
l	liquid
m	mixture
sat	saturation
v	vapour
g	gas
b	bubble
∞	far field
nuc	nucleation
evap	evaporation
cond	condensation
exp	experiment
sim	simulation

Superscripts

p	order of algorithm accuracy

thermal conductivity and evaporation potential in its transcritical state. Employing R744 in refrigeration systems inherently eradicates emissions of greenhouse gas. Overall, heat pump systems based on transcritical CO_2 refrigeration cycles have distinct advantages over traditional fluorine-based refrigerant systems (such as R134a, R410A, etc.), including being pollution-free, efficient, and compact. In recent years, various complex heat pump cycles using transcritical CO_2 as the working medium have been extensively studied to further improve their system efficiency and stability. However, the critical temperature of CO_2 is just 31.2 °C, meaning R744 compression refrigeration systems can only work effectively in transcritical state. Using expansion valves in these systems results in significant throttling losses [11–13] and a sharp decrease in system efficiency. The main loss in transcritical CO_2 refrigeration cycle systems is the irreversible loss caused by phase change after the CO_2 fluid passes through the throttling device, becoming a two-phase fluid. This irreversible loss is significant compared to conventional refrigerants, continually constraining system performance. It is proved that recovering expansion work is an effective means to reduce throttling loss in circulation. The introduction of the ejector [14] can convert pressure energy into kinetic energy to entrain low-pressure working fluid, and then continue to convert it into pressure energy to restore the pressure of low-pressure working fluid. Moreover, the ejector itself has the advantages of simple structure, low cost, no moving parts and easy control of refrigerant flow [15–17], Based on the above advantages and its ability to recover expansion work [18], the ejector has become the key to effectively improve the COP of the transcritical CO_2 refrigeration system. Therefore, it is critical to use ejector in transcritical CO_2 refrigeration system to improve system performance.

In recent years, its ample development prospects have prompted more and more researchers to carry out studies in the fields of transcritical CO_2 heat pumps, especially the optimization of the transcritical CO_2 ejector, and excellent work has begun to emerge in both experimental and simulation fields. Most of the experimental studies coupled simulation means have focused on the performance improvement [19,20], especially the effects of ejector structure on system efficiency. In 2012, Banasiak et al. [21] conducted empirical investigations into the optimal ejector geometric shapes for small-capacity R744 heat pumps. Their findings indicate that ejector efficiency is predominantly influenced by the length and diameter for mixer and the expansion angle. Lawrence et al. [22] conducted a study on controlling the ejector cycle at different ambient temperatures to comprehend the effect of improper control on the capacity of the transcritical CO_2 ejector. Regarding the internal flow behavior of the ejector, the relatively direct method includes experimental measurement. Li's team [23,24] proposed to visualize the two-phase flow using photography, and found the phase change position in the main nozzle, then obtained the pressure data in the nozzle under different conditions through pressure sensors. Zhu et al. [25] made experimental observation on the flow field phenomenon in the mixing chamber and suction chamber of CO_2 ejector. The analysis reveals a direct proportionality between the entrainment ratio and primary expansion angle. Conversely, as the secondary inlet pressure increases, there is a noticeable reduction in the expansion angle. Haghparast et al. [26] employed a combination of experimental and numerical approaches to examine how key size factors and working conditions impact capacity. The research shows that the size of the main nozzle is most crucial affecting the ejector performance and improving the pressure ratio. Zhu [27] found that adding ejector is more effective than the basic system. And the COP of the ejector-expansion system is 10.3% higher than that of the corresponding basic cycle. Liu et al. [28] further optimized the system efficiency, summarizing as follows:

adopting the ejector cycle structure of two-stage evaporation and extreme value seeking control to make the system run at the best exhaust pressure. Compared with the traditional system, the system efficiency is improved by 5.7%. Zhu et al. [29] found that the system capacity and COP can be improved by 11.0% and 8.1% respectively by applying vortex control. Ge et al. [30] discovered that the ejector design using conical-cylindrical mixer can achieve higher efficiency than using cylindrical mixer, and can obtain preferable critical entrainment ratio and compression ratio under distinct working states.

It has to be mentioned, however, that due to the inherent difficulties and complexities of experimental studies, Computational Fluid Dynamics (CFD) has become a crucial tool seeking the flow field inside ejectors [31–33]. More and more researches focus on numerical simulations, which will provide a strong fundamental strategy for further studies of transcritical CO_2 ejectors. Currently, the most commonly used and known mathematical models are: the homogeneous equilibrium model (HEM), homogeneous relaxation model (HRM), the mixture model, and the homogeneous non-equilibrium model with boiling phenomena (HNB) [34–37]. Many researchers have proposed many studies using the above model. The performance analysis of the ejector under variable structure or conditions naturally. Liu et al. [38] established a transient heterogeneous mixture model of CO_2 needle-adjustable ejector, and discussed the mechanism of boundary layer separation, backflow vortex and shock wave to explain the suction flow blocking phenomenon. Li and Deng [39] developed a novel CFD model to investigate the flashing flow in CO_2 ejector. It is found that the prediction error of the model for the secondary mass flow is less than 9%, and the maximum error of the primary mass flow is within 15%. It is important to highlight that although the structure of the ejector is relatively simple, its internal flow behavior is very complicated and changeable, especially the phase transition phenomenon occurring in it has not been fully explored [40]. Colarossi et al. [41] pointed out that the phase change process is driven by turbulence effect and interphase heat transfer, the research revolves around Eulerian simulation method and regards CO2 as a non-thermodynamic equilibrium state. Long et al. [42] proposed a new relaxation drift model (RDM) to simulate the interphase momentum imbalance phenomenon in CO_2 ejector during two-phase work recovery, and the prediction error of RDM for ejector performance is less than 17%, which is less than the maximum error of 23% predicted by HM and ASM. In addition, in the ejector refrigeration cycle system, the evaluation is mostly based on energy-exergy and economic perspectives. Kumar et al. [43] proposed using genetic algorithm to optimize ejector refrigeration system, studied the proposed system with three different refrigerants, then investigated the effects of various operating variables and seasonal changes on the performance and total cost. Abed et al. [44] made a technical and economic analysis on the double ejector-solar-assisted flash tank absorption refrigeration cycle. The results showed that the performance of the cycle system with two ejectors was improved by about 9.2% and 5% respectively under different working conditions. Compared with other configurations, the double ejector cycle is a feasible economic system. Liu et al. [45] designed a new type of cogeneration system, in which the refrigeration cycle of transcritical CO_2 ejector was integrated, and the system sensitivity was analyzed under various conditions to evaluate the thermal and economic relationship between key functional variables and system performance. Habibi et al. [46] carried out numerical simulation in their research work to evaluate the technical and economic performance of air-cooled ejector cooling (ACEC) and ground-coupled ejector cooling (GCEC) systems. The results showed that when a suitable ejector is designed for GCEC system, the seasonal COP reaches 0.343, which is 83% higher than that of ACEC system. Through investigation, it is found that more and more research focused on techno-economic analysis, which will also be one of the focuses of future work.

By analyzing the above literature, it can be found that the performance of CO_2 two-phase ejector is affected by many aspects. In order to truly summarize certain laws of the internal flow characteristics and flow field differences of the ejector, an accurate model is required, as well as the multi-variability of the boundary conditions is indispensable. Therefore, the purpose of this study is to construct a non-equilibrium phase change model considering cavitation-evaporation effect to predict the internal flow of CO_2 two-phase ejector, and calculate it by using the real CO_2 fluid properties. Then, the model is validated by comparing the predicted results with the experimental data. On this basis, the influence law of different working conditions on the overall flow field characteristics and performance is analyzed and summarized. Further, the energy utilization characteristics of two-phase ejector are explored by coupling mass transfer rate and exergy destruction, and the energy efficiency is calculated quantitatively.

Table 1
Detailed data listing of the ejector dimensions.

Geometric parameters	Values for Case1	Value for Case2	Value for Case3
R_{ni} (mm)	3.00	3.00	3.00
R_{th} (mm)	0.45	0.45	0.45
R_{no} (mm)	0.51	0.51	0.51
R_{mix} (mm)	1.50	1.00	2.50
R_{ex} (mm)	4.00	3.00	5.00
L_{nd} (mm)	3.44	3.44	3.44
L_{sc} (mm)	3.60	4.90	1.00
L_{mix} (mm)	15.00	20.00	50.00
L_{diff} (mm)	57.26	45.79	57.26
θ_{nc} (°)	15.0	15.0	15.0
θ_{sn} (°)	21.0	21.0	21.0
θ_{diff} (°)	2.5	2.5	2.5

2. Numerical modeling

2.1. Ejector geometry

Traditional ejectors consist of four components: a power nozzle, a suction chamber, a mixing chamber, and a diffuser. In this study, the ejector dimensions provided in Banasiak's literature [47] are utilized for the ejector geometries, which serves as the computational basis. To optimize computational resources, the geometry of all ejectors is simplified into two-dimensional axisymmetric structures.

Following the experimental results presented in the literature, ejector geometries and testing are conducted for three distinct cases, each with specific dimensions. For enhanced data support and visual representation, the dimensions of the ejector are depicted in Table 1, with the structure of Case 1 being illustrated in Fig. 1.

2.2. Mathematical model

Complex flow behavior inside a two-phase ejector needs to rely on mathematical formulas for its description. In this section, the mathematical foundations will be itemized and clarified [48–50].

2.2.1. Governing equations

For the scenario of transcritical CO_2 two-phase flow, the Mixture model is selected for the two-phase flow modeling. The key parameters of the fluid within the ejector, such as velocity, pressure, and the distribution of the two-phase volume fraction, will be obtained by solving the conservation equations of mass, momentum, energy, and the volume fraction of the gas phase.

$$\frac{\partial}{\partial t}(\rho_m) + \nabla\cdot(\rho_m u_m) = 0 \tag{1}$$

In this formula, subscript m stands for mixture, ρ_m(kg/m^3) stands for mixture density, and u_m(m s^{-1}) stands for mixture velocity.

$$\frac{\partial}{\partial t}(\rho_m u_m) + \nabla\cdot\left(\rho_m u_m u_m{}^T\right) = -\nabla \mathrm{p} + \nabla\left[\mu_m\left(\nabla u_m + \nabla u_m{}^T\right)\right] + \rho_m g \tag{2}$$

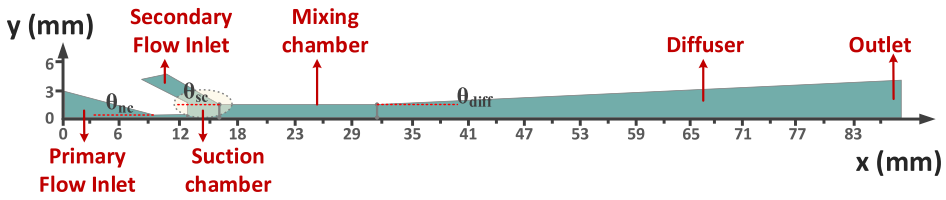

Fig. 1. The geometric structure and size description of ejector (Case1 as an example).

where the μ_m(Pa·s) represents the viscosity, p(Pa) is the pressure for the flow field. And the g(m s^2) can be described as the acceleration of gravity.

$$\frac{\partial}{\partial t}\sum_{k=1}^{n}(\alpha_k\rho_k E_k)+\nabla\cdot\sum_{k=1}^{n}(\alpha_k u_k(\rho_k E_k+p))=\nabla\bullet\left(k_{eff}\nabla T\right)+S_E \tag{3}$$

Similarly, k_{eff}(W/(m·K)) is the effective thermal conductivity, and α_k is defined as the volume fraction, and the subscript k represents different phases in the mixture model.

The volume fraction of gas phase can be expressed as:

$$\frac{\partial}{\partial t}(\alpha_g\rho_g)+\nabla\cdot\left(\alpha_g\rho_g\vec{u}_g\right)=\dot{m}_{evap}-\dot{m}_{cond} \tag{4}$$

In the formula, $\dot{m}_{evap}$ and $\dot{m}_{cond}$ (kg m^{-3} s^{-1}) respectively represent the mass transfer per unit volume between gas and liquid phases due to evaporation and condensation; In addition, subscripts g and l stand for the phase of gas and liquid. The average value of density and velocity of mixed flow can be expressed as:

$$\rho_m=\alpha_l\rho_l+\alpha_g\rho_g \tag{5}$$

$$u_m=\frac{\alpha_l\rho_l u_l+\alpha_g\rho_g u_g}{\rho_m} \tag{6}$$

E_k (J/kg) is the total energy, and the expression can be defined as:

$$E_k=h_k-\frac{p}{\rho_k}+\frac{u_k^2}{2} \tag{7}$$

S_E is the user-defined energy source term (energy exchange between gas and liquid), where h (J/kg) is the latent heat of evaporation.

$$S_E=\dot{m}\cdot h \tag{8}$$

2.2.2. Phase change models

The model holds that the two phases can be well mixed, that is, it is assumed that the two-phase medium is evenly mixed and the gas-liquid two phases have the same flow velocity; The mixed phase is in thermal equilibrium, and it is considered that the mass transfer between the two phases is instantaneous. The mass transfer rate was derived by Zwart-Gerber-Belamri et al. [39]. The phase change mechanism of the primary nozzle was explained in terms of cavitation and evaporation process. The behavior of bubbles can be described by the Rayleigh-Plesset equation:

$$R_B\frac{D^2R_B}{Dt^2}+\frac{3}{2}\left(\frac{DR_B}{Dt}\right)^2=\frac{p_b-p_\infty}{\rho_l}-\frac{4\mu_l}{R_B}\frac{DR_B}{Dt}-\frac{2\sigma}{\rho_l R_B} \tag{9}$$

where R_B (m) represents the radius of the bubble. p_b is the bubble pressure. And p_∞ is the pressure away from the bubble. ρ_l is the liquid density. μ_l is kinematic viscosity of the liquid, and σ(N/m) represents the surface tension of the liquid.

The above equation can be simplified if the second order derivative term and surface tension are neglected:

$$\frac{DR_B}{Dt}=\sqrt{\frac{2}{3}\frac{p_b-p_\infty}{\rho_l}} \tag{10}$$

Furthermore, the mass change rate of bubbles is:

$$\frac{dm_B}{dt}=\rho_g\frac{dV_B}{dt}=\rho_g\frac{d\left(\frac{4}{3}\pi{R_B}^3\right)}{dt}=4\pi{R_B}^2\rho_g\sqrt{\frac{2}{3}\frac{p_b-p_\infty}{\rho_l}} \tag{11}$$

where V_B represents the volume of the bubble.

In this study, assuming that all bubbles have the same radius. The relationship between gas volume fraction α_g, bubble number n and bubble radius R_B is as follows:

$$\alpha_g=n\times\left(\frac{4}{3}\pi{R_B}^3\right) \tag{12}$$

By combining Formula (11) and Formula (12), it can be calculated that the interphase mass transfer value of the total bubbles per unit volume is,

$$\dot{m}=n\frac{dm_B}{dt}=\frac{3\alpha_g\rho_g}{R_B}\sqrt{\frac{2}{3}\frac{p_b-p_\infty}{\rho_l}} \tag{13}$$

The increase in the volume fraction of vapour is accompanied by the corresponding decrease in the density of the vapour core position in the vaporization process, so the volume fraction of vapour in formula (13) is modified, and α_g in the bubble formation equation is replaced by $\alpha_{nuc}(1-\alpha_g)$. Consequently, the mass transfer rate in gas and liquid phase of Zwart-Gerber-Belamri cavitation phase change model can be described as [51]:

$$if\ p<p_v, \dot{m}_{evap}=C_{evap}\frac{3\alpha_{nuc}(1-\alpha_g)\rho_g}{R_B}\sqrt{\frac{2}{3}\frac{p_v-p_\infty}{\rho_l}} \tag{14}$$

$$if\ p>p_v, \dot{m}_{cond}=C_{cond}\frac{3\alpha_g\rho_g}{R_B}\sqrt{\frac{2}{3}\frac{p_\infty-p_v}{\rho_l}} \tag{15}$$

where $\dot{m}_{evap}$ represents the mass change rate during bubble generation process, while $\dot{m}_{cond}$ represents the mass change rate during bubble collapse process. In addition, α_{nuc} in the formula is defined as the volume fraction at the nucleation site.

p_v is the threshold pressure (saturated vapour pressure) in the process of cavitation, which can be defined as:

$$p_v=p_{sat}+\frac{1}{2}(0.39\rho_m k) \tag{16}$$

where the p_{sat} can be determined by the saturation pressure corresponding to the local temperature. The k (m^2/s^2) is treated as turbulence kinetic energy.

Lee model [52] is adopted to simulate internal evaporation phase change behavior in the ejector:

$$if\ T_l>T_{sat}, \dot{m}_{evap,Lee}=C_{evap,Lee}\alpha_l\rho_l\frac{(T_l-T_{sat})}{T_{sat}} \tag{17}$$

$$if\ T_g<T_{sat}, \dot{m}_{cond,Lee}=C_{cond,Lee}\alpha_g\rho_g\frac{(T_{sat}-T_g)}{T_{sat}} \tag{18}$$

where $C_{evap,Lee}$ and $C_{cond,Lee}$ are the semi-empirical coefficient. Similarly,

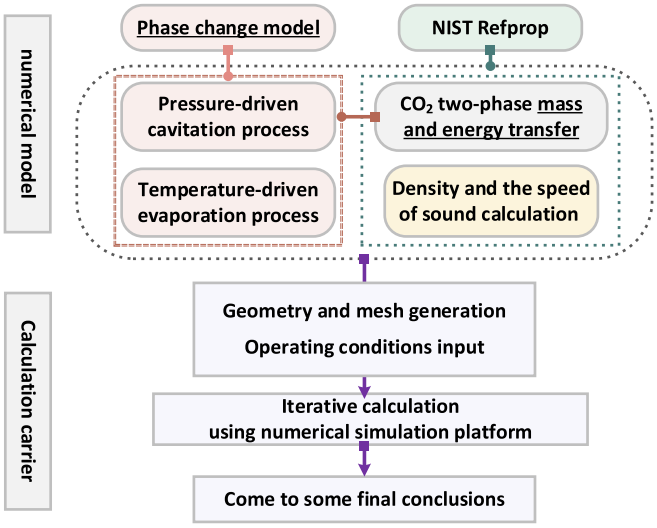

Fig. 2. Schematic diagram of the calculation process.

subscripts evap and cond stand for evaporation and condensation respectively. And T_{sat} (K) is saturation temperature.

Additionally, the speed of sound for mixed fluid is a key link in calculating the Mach number of fluid flow fields. This study will mainly present two methods for calculating the speed of sound c (m s^{-1}), one of which is:

$$c = \sqrt{\frac{1}{(\alpha_l\rho_l + \alpha_g\rho_g)\left(\frac{\alpha_l}{\rho_l a_l^2} + \frac{\alpha_g}{\rho_g a_g^2}\right)}} \tag{19}$$

The above calculation assumes that there is no mass exchange between the two phases, which obviously does not conform to the basic assumption of this study. Therefore, it is decided to apply the second calculation method of speed of sound. Brennen [53] presented another method for calculating the speed of sound in gas-liquid two-phase flows, specifically the following formula:

$$\frac{1}{\rho_m c^2} = \frac{\alpha_g}{p}\left[(1-\varepsilon_g)f_g + \varepsilon_g g_g\right] + \frac{\alpha_l}{p}\left[(1-\varepsilon_l)f_l + \varepsilon_l g_l\right] \tag{20}$$

In this formula, f_g is approximately equal to 1, f_l is approximately equal to 0, and g_g is approximately equal to 1. Furthermore, ε_g is approximately equal to $(1-\alpha_g)$, and ε_l is approximately equal to α_g.

$$g_l = 2.1\left(\frac{p}{p_{crit}}\right)^{-0.566} \tag{21}$$

Therefore, the final form of the Brennen equation can be described as:

$$c = \sqrt{\frac{1}{\rho_m\left(\frac{\alpha_g}{p} + 2.1\frac{\alpha_g\alpha_l}{p}\left(\frac{p}{p_{crit}}\right)^{-0.566}\right)}} \tag{22}$$

2.3. Solution setup

The calculation framework of this study is based on Fluent software, and coupled with C/C++ code to discretize the flow field parameters, integrating a non-equilibrium phase change model established through coupling user-defined functions (UDF) with the simulation software. The research employs a mixture model, where the primary flow is designated as a supercritical fluid, and the secondary flow is treated as a superheated gas. Considering the complexity of the variation in thermophysical properties of the working fluid under supercritical conditions, a real gas model is employed for simulation calculations. Temperature and pressure are used as independent variables, and the interpolation expansion of superheated liquid region is realized by using the property table extracted from NIST Refprop software library to meet the complexity and instability of physical property changes during liquid-gas transformation. Then, according to the data extracted from NIST Refprop, the script of CO_2 density and speed of sound is written, thus improving the accuracy and effectiveness of calculation. Additionally, to economize on computational resources, an axisymmetric computational domain is chosen. The pressure inlet and pressure outlet conditions are specified as the boundary conditions. The flow field computation adopts the SST k-ε turbulence model, and a pseudo-transient pressure-based solver is selected. The Coupled approach is implemented in the pressure-velocity coupling scheme, with gradient and pressure spatial discretization employing the Least Squares Cell Based and PRESTO! methods, respectively. The logic diagram (part) of the calculation strategy is displayed in Fig. 2.

3. Model validation

3.1. Grid generation

According to the size parameters of the three ejectors provided by Table 1, the grid generation is carried out in ICEM. The three grids are shown in the following Fig. 3. For a tidier display, the diffuser part of the ejector is primarily shown for case2, while case1 and case3 are truncated because of their long diffusers. In order to meet the requirements of calculation cost and accuracy, the grid independence verification test is carried out. Taking case1 as an example, in order to obtain the best computational grid, three groups of grids are calculated and analyzed by GCI: a: Fine (165,200 quadrilateral elements), b: Medium (119,665 quadrilateral elements) and c: Coarse (87,500 quadrilateral elements). The calculation formula of GCI is as follows:

$$GCI = \frac{F_s|\varepsilon|}{r^p - 1} \times 100\% \tag{23}$$

Taking the outlet pressure as the test parameter, the specific results

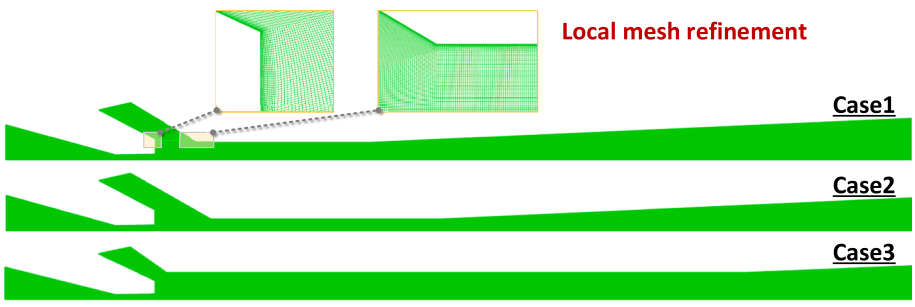

Fig. 3. Mesh generation and local refinement for three cases (truncation exists in the diffuser section).

Table 2
The GCI test results.

	F_s	3
	p	3
Grids (a,b)	$\varepsilon_{a,b}$(%)	0.16
	$GCI_{a,b}$(%)	0.79
Grids (b,c)	$\varepsilon_{b,c}$(%)	0.67
	$GCI_{b,c}$(%)	2.33

Table 3
Description of the boundary conditions for the three cases of the validation session.

Operating Conditions	Case1	Case2	Case3
$p_{p,in}$ (MPa)	8.01	8.49	8.07
$T_{p,in}$ (K)	303.7	303.8	303.7
$p_{s,in}$ (MPa)	3.56	3.56	3.55
$T_{s,in}$ (K)	278.3	302.5	279.2
p_{out} (MPa)	3.9	3.59	3.67

are shown in the Table 2. Accordingly, the number of grids in case2 is relatively small, and the final number of grids is 108,221, while the number of grids in case1 and case3 is 119,665 and 138,541 respectively. To achieve higher computational accuracy, local grid refinement was conducted near the wall surfaces and around the power nozzle of the ejector, and the mathematical model is validated by using these three different mesh structures as calculation carriers.

3.2. Accuracy calculation

The validation of pressure data at specific locations along the ejector was carried out first. It should be noted that the ejector dimensions and experimental data of the validation part of this study come from Banasiak [47], which is also an important basis to prove the accuracy of the numerical model of this study. The simulation operating conditions of case1, case2 and case3 are listed in the Table 3. As shown in the Fig. 4 below, the four specific locations are at the inlet, center, outlet in the mixing chamber and the center of the diffuser. For case1, the maximum relative error (MRE) 16.43% in pressure compared with the experimental data exists at the entrance of the mixing chamber. For case2, the MRE between the two in the exit of the mixing chamber, with a value of 11.66%, while for case3, the predicted pressure data is in high agreement with the experimental data, with a value between the two of only 2.11%. So far, the MER of the pressure distribution is within the acceptable range, which initially confirms that the mathematical model developed in this study and the numerical computation strategy employed are capable of predicting the behavior of the flow field inside the CO_2 two phase ejector. In order to further confirm our ideas, it was decided to perform an error analysis of the mass flow rate under the same three structures.

The relative error (RE) in this can be calculated by:

$$RE = \frac{y_{exp} - y_{sim}}{y_{exp}} \times 100\% \tag{24}$$

where y_{exp} is experimental measurement data and y_{sim} is simulation data.

As shown in the Fig. 5 below, the boundary conditions in the table are still maintained. The blue column represents the experimental data and simulation data of m_p, while the red column represents the experimental data and simulation data of m_s. Under the condition of Case1, the MRE between the experimental value and the predicted value of m_p is 2.29%, while the error value of secondary flow between them is only 0.32%. In Case2, the MRE in the primary and secondary flow between the experimental and simulated values are 5.81% and 13.82% respectively, and under Case3 these two error values become 4.81% and 4.8%. That is to say, the calculation results validated by three different structures and different boundary conditions are all within a reasonable error range, and the accuracy is high. Therefore, the mathematical model and numerical calculation method established in this study are feasible, which can further predict and analyze the internal flow characteristics and flow field behavior of transcritical CO_2 two phase ejectors.

4. Results and discussion

From the above verification process, it is decided to analyze the different entrance conditions. The internal flow behavior of CO_2 two phase ejector is complex, involving variable flow field phenomena, and different operating conditions will have a great impact on the ejector performance. Therefore, it's very necessary and instructive to clarify the variation law of performance with variable inlet conditions. It should be noted in advance that all the boundary condition settings of the ejector are shown in the following Table 4.

4.1. Two-phase flow behavior

According to the structure, the mixing chamber length of the ejector in Case3 is much longer than that of the ejectors in Case1 and Case2, which will cause the expansion work to be more dependent on the turbulent dissipation, and may also cause a strong expansion impact at the nozzle outlet. At the same time, the diameter of the mixing chamber and the length of the diffuser of the ejector in Case2 are small, which may lead to insufficient mixing of the two fluids and insufficient time for pressure recovery. Therefore, further research will proceed based on the structure of Case 1. Analysis on the flow field characteristics will play a certain guiding role in exploring the performance evolution laws. Therefore, this section will focus on analyzing the flow behavior inside the ejector under the different inlet boundary conditions mentioned above.

First of all, still under variable back pressure conditions, Fig. 6 below shows the pressure distribution along the ejector at different back pressures. In the suction chamber, the pressure oscillates, and as the back pressure increases, the oscillation phenomenon in the latter half of the suction chamber is alleviated. In addition, higher back pressure conditions lead to higher pressure in the mixing chamber. It is observed that when the back pressure is 3.58 MPa and 3.60 MPa, the inlet pressure of the constant area mixing chamber is close to coinciding, indicating that the back pressure is around the critical value. However, when the back pressure is between 3.65 MPa–4.0 MPa, the inlet pressure at the mixing chamber increases accordingly, approaching or even exceeding the secondary inlet pressure. This can severely affect the ability of ejector to pump secondary flow, and may even lead to failure of entrainment or backflow.

Worthy of attention is that the analysis of flow field characteristics under varying primary inlet pressure conditions is also crucial for analyzing its injection performance. Fig. 7 (a) below shows the pressure contour distribution under the primary inlet pressure, including the minimum and maximum pressure conditions (8.01 MPa and 10.71 MPa respectively). Taking two extreme pressure conditions as examples, it can be clearly observed after amplification that with the continuous increase of primary inlet pressure, shock waves will form at the outlet of the ejector nozzle, creating low pressure regions with areas lower than the secondary inlet pressure, thereby continuously intensifying the throttling effect and leading to the decline of the ejector performance. Fig. 7 (b) exhibits the axial distributions of gas phase volume fraction and density throughout the mixing chamber (with inlet pressures of 8.46 MPa, 8.91 MPa and 9.36 MPa, respectively). It can be seen that the elevation of primary inlet pressure will result in a decrease in the gas phase volume fraction in the mixing chamber, signifying that the increase of primary mass flow rate remains in a dominant/prevailing state. Because the liquid phase density of CO_2 is much higher than its gas phase density, the mixed density will rise with the increase of pressure.

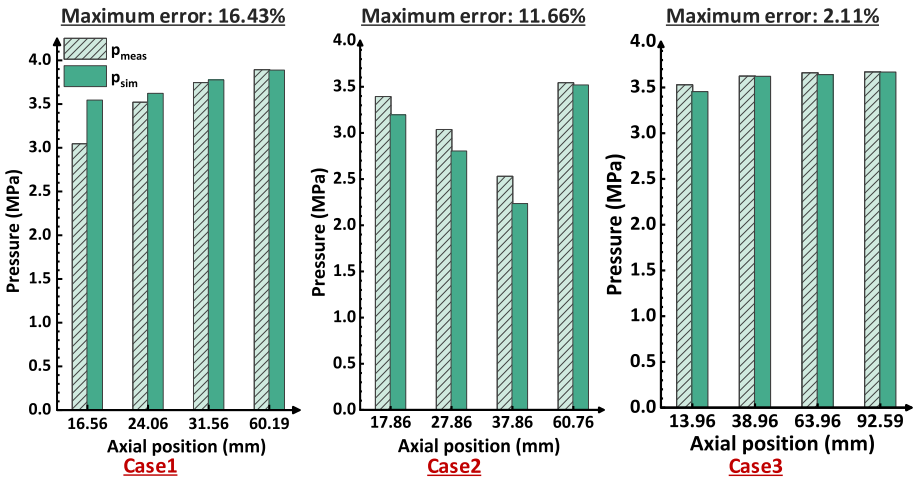

(a) Comparison of experimental data and simulation value at specific axial position of ejector

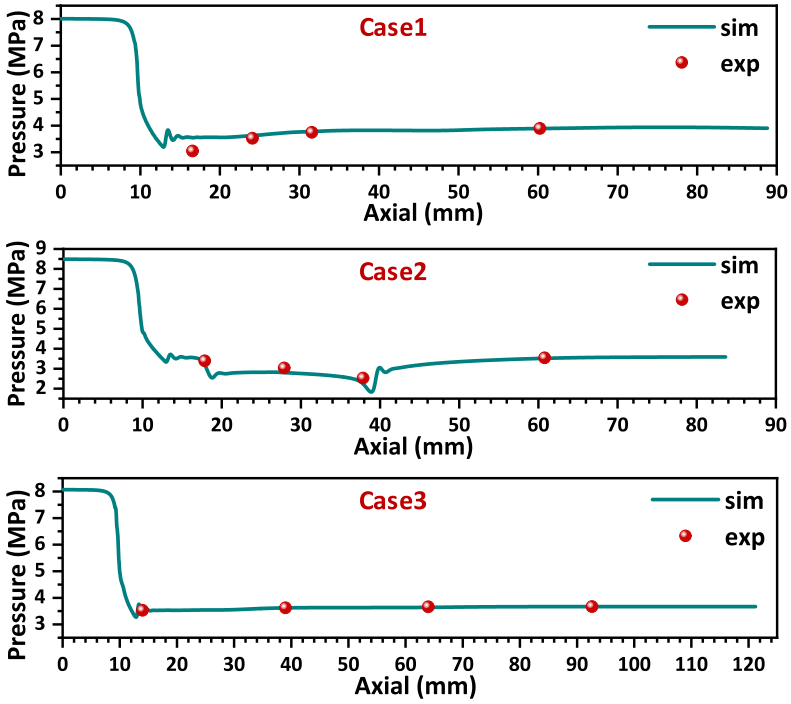

(b) Pressure distribution at the axis of ejector

Fig. 4. Comparison of experimental data and simulation values of ejector.

It is also worth pointing out that there are certain differences in the velocity distribution profiles under different $p_{p,in}$. As shown in Fig. 8, it can be observed that the mixture velocity inside the ejector is relatively uniform. There is an obvious acceleration stage inside the primary nozzle. After passing through the mixing chamber, the velocity gradually decreases, that is, the kinetic energy of the two-phase flow is more effectively converted into pressure potential energy inside the diffuser. With the increase of $p_{p,in}$, both the amplitude of velocity and the area of high-speed region in the entire mixing chamber will increase. This phenomenon will cause the initial velocity at the inlet of the diffuser to rise, that is, there will be a larger residual flow velocity in the expander, thus resulting in further acceleration and pressure drop.

As shown in the Fig. 9, with the rise of primary inlet temperature (while keeping other conditions unchanged, including the primary inlet pressure, secondary inlet pressure, and outlet pressure listed in the figure), the distribution law of the volume fraction for gas phase and the mixed density is different from that of primary pressure $p_{p,in}$. The raise of the primary inlet temperature causes a slight increase in the dryness of the fluid, that is, an increase in the gas phase content in the mixed fluid, while the primary flow mass flow rate decreases. Given that the density of liquid CO_2 is higher than that of gaseous CO_2, when the dryness of the fluid increases, the density of the mixed fluid decreases. Moreover, its density and volume fraction remain oscillating throughout the mixing chamber, indicating that complex heat and mass transfer are occurring. This phenomenon exists under any variable operating conditions.

Furthermore, an intriguing phenomenon observed with the alteration of boundary conditions is the phase change process. In this study, mass transfer rate is defined as the net mass generation in the evaporation phase change process, which calculating through external self-compiled code. In order to explain the internal reason of the change of gas-liquid integral number more intuitively, Fig. 10 illustrates the distribution of mass transfer rate curves during evaporation under varying primary inlet temperatures and outlet back pressures. The treatment method is: the starting position is 8.52 mm, the distance from the end

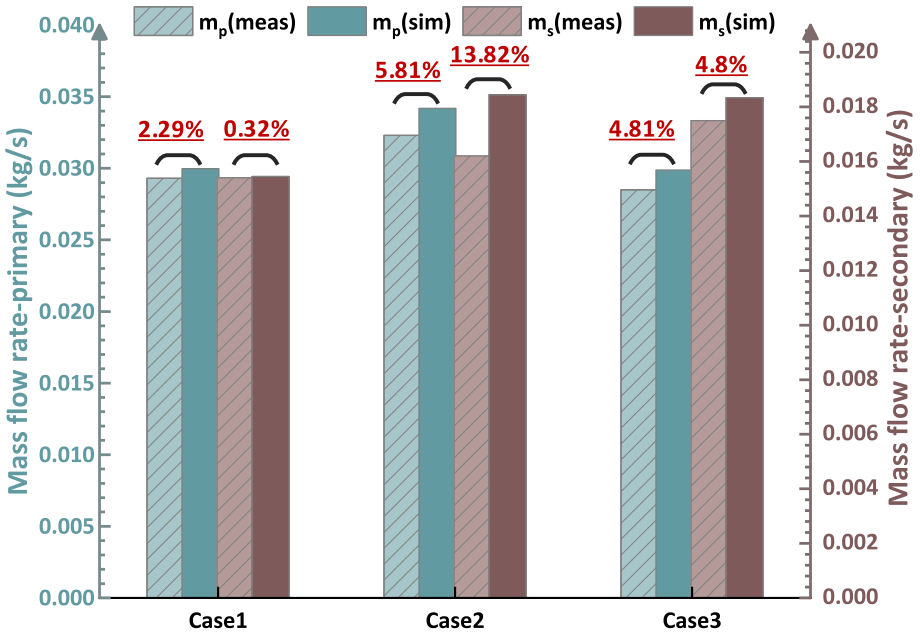

Fig. 5. Error analysis of experimental value and simulation value of primary and secondary flow mass flow.

Table 4
The setting of ejector working conditions.

$p_{p,in}$ (MPa) $p_{s,in} = 3.56$, $p_{out} = 3.90$, $T_{p,in} = 303.7$	p_{out} (MPa) $p_{p,in} = 8.01$, $p_{s,in} = 3.56$, $T_{p,in} = 303.7$	$T_{p,in}$ (K) $p_{p,in} = 8.46$, $p_{s,in} = 3.56$, $p_{out} = 3.90$
7.56	3.58	303.7
8.01	3.60	308.7
8.46	3.65	313.7
8.91	3.70	
9.36	3.80	
9.81	3.90	
10.00	4.00	
10.71		

point is 11.52 mm, and there are 25 sections in increments of 0.125 mm (in order to make the data more detailed, the increment before and after the throat is reduced to 0.03125 mm when the back pressure changes), and then the average value of mass change rate of each surface is calculated. It can be seen that no matter what kind of conditions (involved in this study), intensive mass transfer occurs near the throat, but under different boundary conditions (including supercritical state), the location and value of this phenomenon are obviously different.

In the Fig. 10(a), when the inlet pressure is kept at 8.46 MPa, as the temperature rises from 303.7 K to 308.7 K, it means that the primary flow CO_2 changes from subcritical state to supercritical. It can be clearly seen that the maximum mass change rate in subcritical state appears at the nozzle throat, and the value is $2.25*10^7$ kg/m^3/s. When the temperature rises to 308.7 K, evaporation occurs before the throat (about 9.27 mm), the value is about $3.51*10^7$ kg/m^3/s, and then another obvious mass transfer occurs at the throat. Finally, when the primary

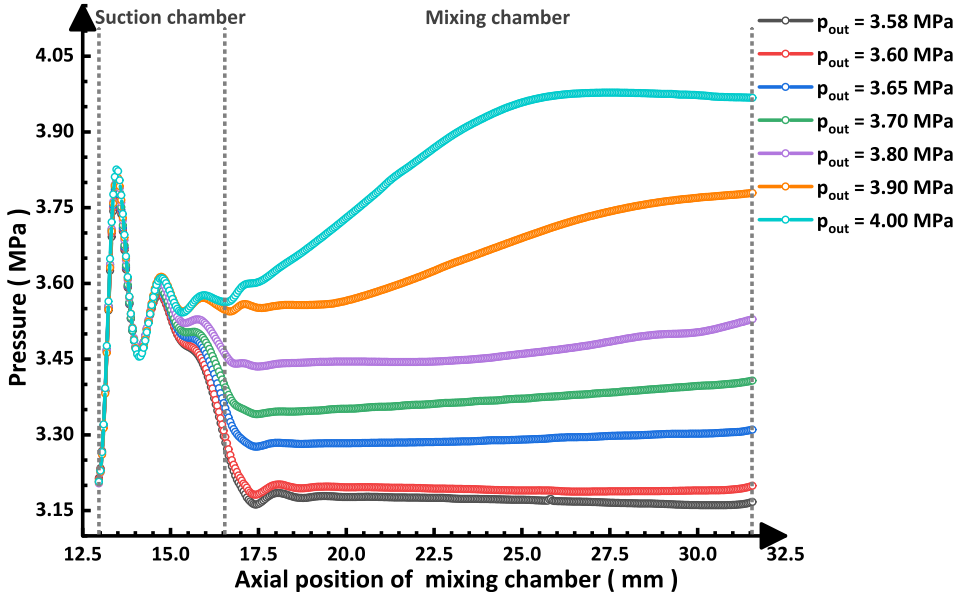

Fig. 6. Pressure distribution curve in mixing chamber under variable back pressures.

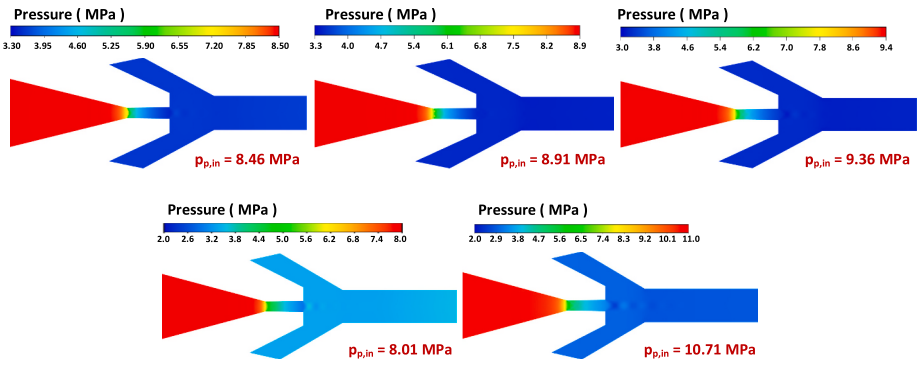

(a) Profile distribution of Pressure

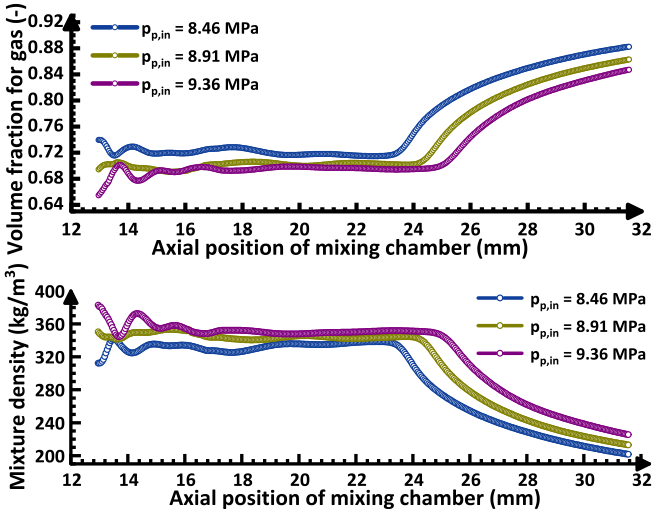

(b) Axial distribution of density and volume fraction

Fig. 7. Analysis of pressure, volume fraction and density under different primary pressures.

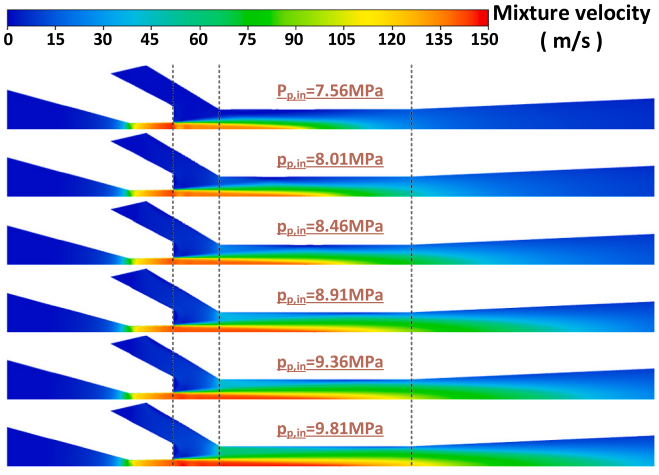

Fig. 8. Comparison velocity contour maps under different inlet pressure conditions.

inlet temperature increased to 313.7 K, evaporation occurred in a more forward position (about 9.02 mm). The maximum value during evaporation appeared in the nozzle throat, which was 7.69 × 10^7 kg/m^3/s. Then, the average mass change rate under the condition of changing back pressure was calculated by taking p_{out} as 3.6, 3.7 and 3.8 MPa respectively. The results in Fig. 10(b) show that, other conditions remain the same, with the increase of back pressure, stronger evaporation mass transfer phenomenon will appear at the back of the nozzle throat. For example, when the back pressure is 3.8 MPa, the maximum evaporation mass change rate at about 9.55 mm with the value is 3.96*10^7 kg/m^3/s relative to 3.6 MPa.

4.2. Ejector performance

Taking the above analysis of flow field characteristics as the foundation the entrainment performance under different conditions will be calculated.

4.2.1. Effect of the outlet pressure

Fig. 11 illustrates the variation trend in entrainment ratio ($ER = m_s/m_p$) under variable back pressure, with the inlet pressures of the primary and secondary flows held constant at 8.01 MPa and 3.56 MPa, respectively. The data demonstrates that for a given ejector, there exists a critical back pressure value when the primary and secondary inlet pressures are fixed. This critical back pressure is in close proximity to the pressure of the entrainment flow. Before reaching this critical back pressure threshold, the ejector remains in a double choked state, meaning the entrainment ratio does not respond to changes in outlet pressure. However, once this critical point is exceeded, the ejector rapidly transitions to a single choked state, causing the entrainment ratio to sharply decline. At even higher back pressures, the ejector may reach a reflux state, at which point the entrainment ratio will be less than zero.

The existence of this critical back pressure highlights the sensitivity

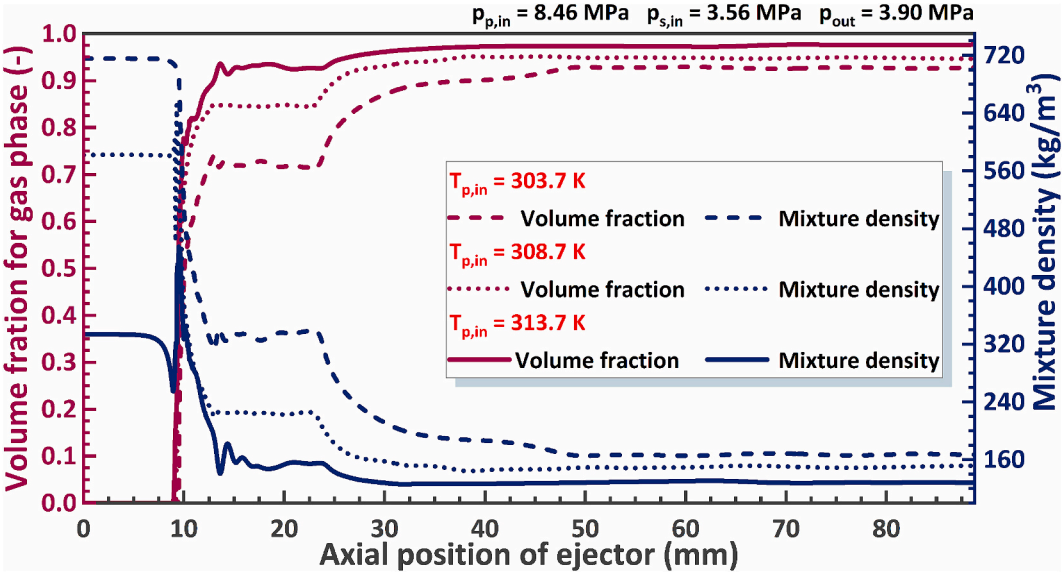

Fig. 9. Comparison of axial distribution of gas volume fraction and mixture density at different primary inlet temperatures.

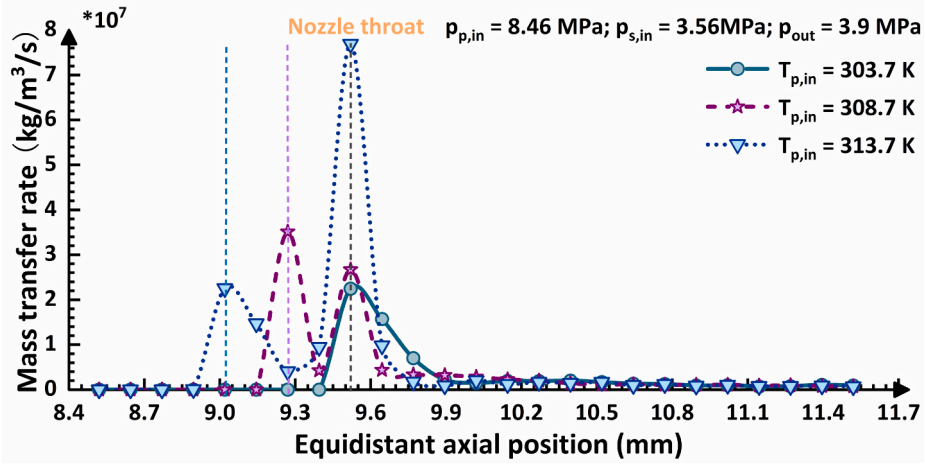

(a) Mass transfer rate under primary temperature change

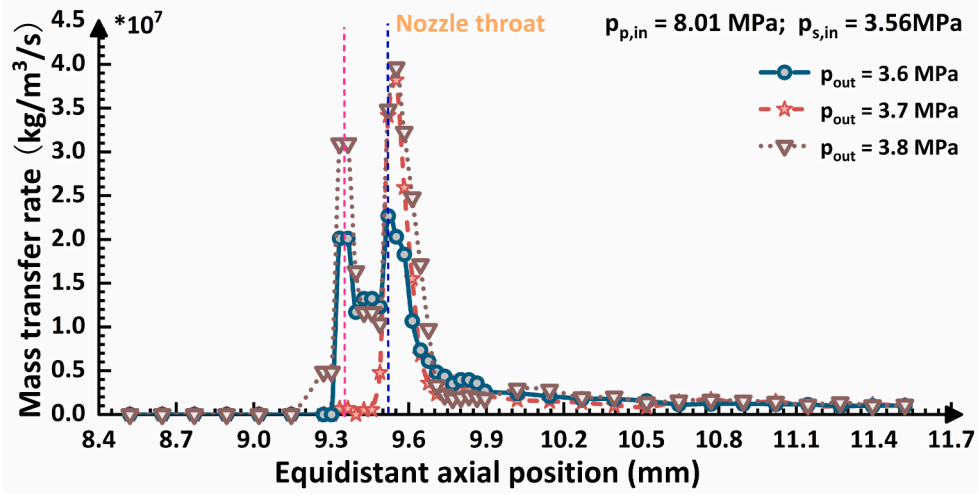

(b) Mass transfer rate under change of back pressure (partial)

Fig. 10. Analysis of mass transfer rate in evaporation process under variable operating conditions.

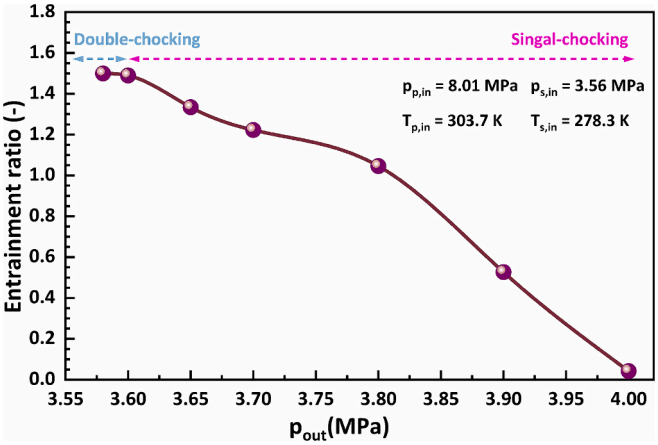

Fig. 11. Trend of entrainment ratio under different back pressure conditions.

of the entrainment ratio to outlet pressure near choked conditions. Further analyses of the transition point and entrainment ratio response could elucidate the underlying flow physics and choked flow mechanisms relevant to this type of ejector system.

4.2.2. *Effect of the primary pressure*

To verify the influence of $p_{p,in}$ on ejector performance, $p_{p,in}$ is changed to obtain different entrainment ratios. As shown in Fig. 12, when the secondary flow pressure and outlet pressure are kept at 3.56 MPa and 3.90 MPa respectively, it can be seen that when the primary inlet pressure changes between 7.56 MPa and 10.71 MPa, the entrainment ratio basically increases with the raise of pressure, however, the rising rate dropped significantly. Of course, at this time, the values of primary flow mass flow and secondary flow mass flow are increasing, and as quantitatively indicated through the informative column chart, the magnitude of enlargement occurring in the secondary flow mass flow is notably and consistently greater than that in the primary flow mass flow at each pressure point. Subsequently, the inlet pressure of the primary flow continued to increase, and although the entrainment ratio was still rising, it was obvious that the growth rate had decreased. This is because, with the increase of primary pressure, the primary mass flow will continue to increase even more. Finally, the entrainment ratio will begin to show a downward trend after the peak value appears. When the primary inlet pressure increases to 10.71 MPa, the entrainment rate decreases by 0.014 compared with 9.81 MPa.

4.2.3. *Effect of the primary temperature*

An increase in the inlet temperature can also have a significant effect on the entrainment ratio of the ejector. In this study, three temperature conditions were selected, with increments of 5 K, where the primary pressure, secondary pressure and outlet pressure were kept constant at 8.46 MPa, 3.56 MPa and 3.9 MPa. The secondary inlet temperature also remained unchanged at 278.3 K. The specific prediction results are listed in Fig. 13. As shown, with the increase for primary temperature, the entrainment ratio exhibits a linear increasing trend. However, unlike

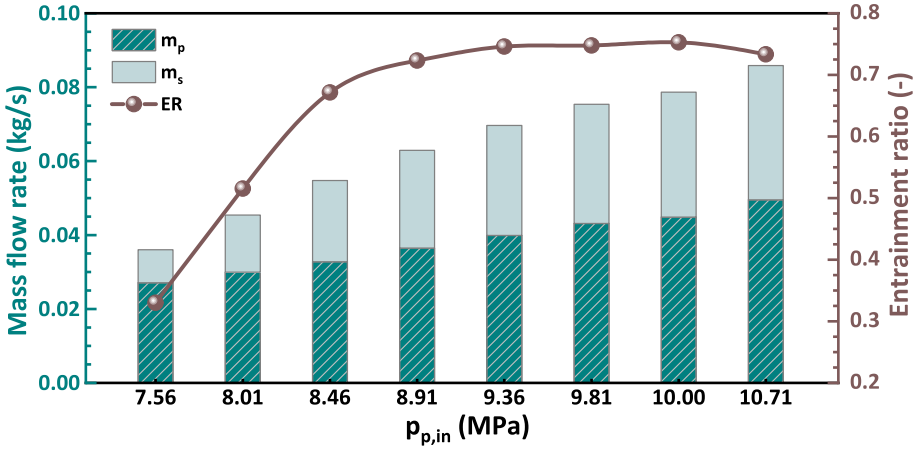

Fig. 12. Difference of entrainment ratio and mass flow rate under variable primary inlet pressure.

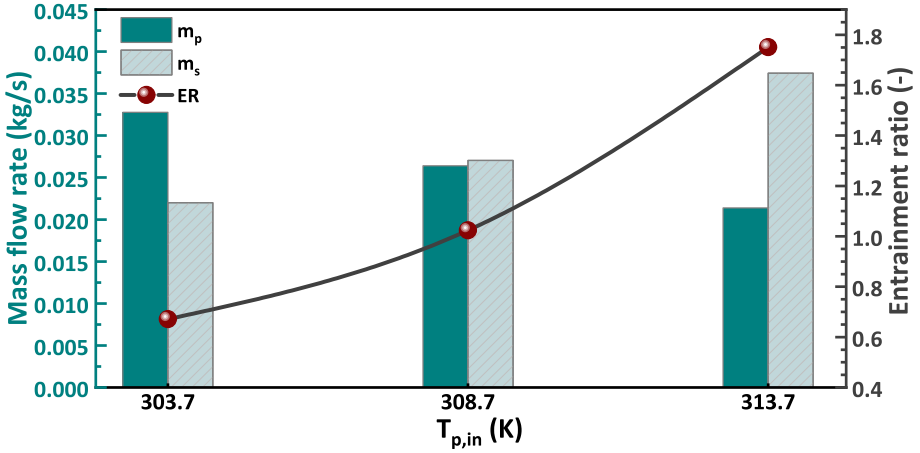

Fig. 13. Difference of entrainment ratio and mass flow rate under variable primary inlet temperature.

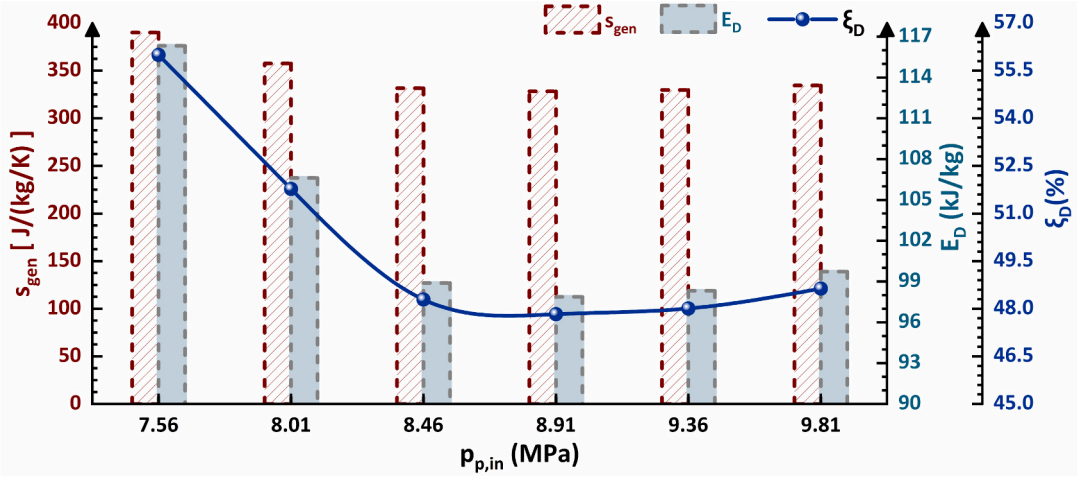

(a) Values of s_{gen}, E_D and ξ_D under variable primary pressure

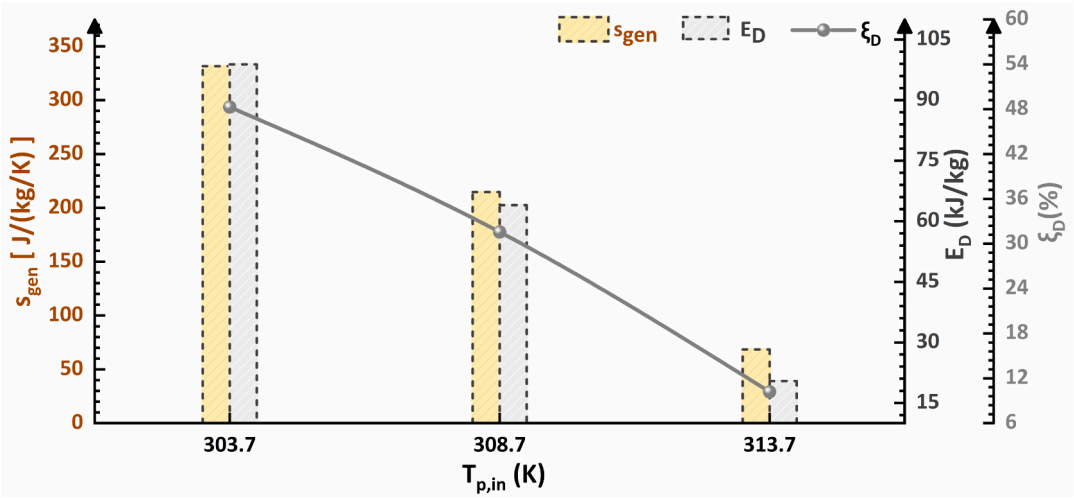

(b) Values of s_{gen}, E_D and ξ_D under variable primary temperature

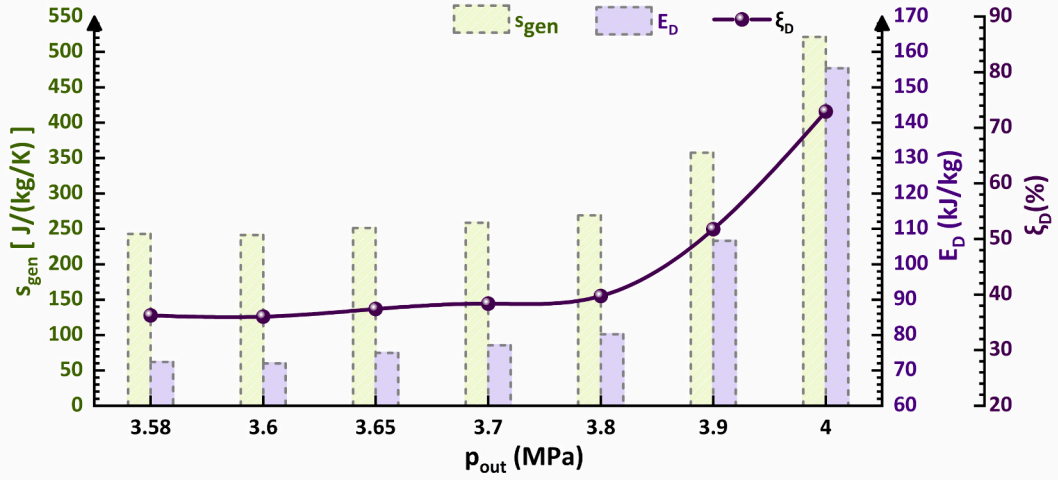

(c) Values of s_{gen}, E_D and ξ_D under variable outlet pressure

Fig. 14. Calculation of entropy generation, exergy destruction and exergy destruction ratio.

Table 5
Detailed data of s_{gen}, E_D and η in the ejector under variable OC.

Operating Conditions		s_{gen} (J/kg K^{-1})	E_D (kJ/kg)	ξ_D	Efficiency (η_{ej})
$p_{p,in}$ (MPa)	7.56	390.17	116.27	0.565	0.13
	8.01	357.59	106.56	0.520	0.21
	8.46	331.66	98.84	0.483	0.27
	8.91	328.30	97.83	0.478	0.28
	9.36	329.75	98.27	0.480	0.28
	9.81	334.50	99.68	0.486	0.27
$T_{p,in}$ (K)	303.7	331.66	98.84	0.483	0.27
	308.7	214.68	63.97	0.316	0.30
	313.7	68.56	20.43	0.102	0.31
p_{out} (MPa)	3.58	242.86	72.37	0.363	0.54
	3.6	241.46	71.96	0.360	0.54
	3.65	251.39	74.91	0.374	0.49
	3.7	258.65	77.08	0.384	0.46
	3.8	269.12	80.20	0.398	0.41
	3.9	357.59	106.56	0.518	0.21
	4.0	521.23	155.33	0.729	0.018

changes in the primary pressure, an increase in the primary temperature will lead to a smaller primary mass flow rate, but the secondary mass flow rate is still in an obvious increasing trend. That is to say, the increase of the primary inlet temperature brings about a larger dryness fraction of the primary flow.

4.3. Energy efficiency evaluation

Except the investigation of the fixed flow field characteristics, the investigation of the internal energy of the ejector will also be a key link to clarify its working performance. In this study, the concepts of entropy generation (s_{gen}) and exergy are introduced to calculate. Entropy generation is caused by the irreversibility in the system. The greater the irreversibility, the greater the entropy generation, and therefore the exergy of destruction (E_D) will also increase. And some necessary mathematical descriptions need to be given.

The specific exergy is defined as:

$$E_X = h_{in}^* - h_0 - T_0\left(s_{in}^* - s_0\right) \tag{25}$$

where the subscript 0 represents the reference environmental state value. The exergy destruction E_D of ejector can be calculated in this study by

$$E_D = T_0 s_{gen} = T_0\left(s_c - \frac{1}{1+E_R}s_p - \frac{E_R}{1+E_R}s_s\right) \tag{26}$$

where the s_{gen} is the entropy generation. Subscripts p, s and c represent the primary inlet, secondary inlet and outlet of the ejector respectively.

Then, the expression of exergy destruction ratio is:

$$\zeta_D = \frac{(1+E_R)E_D}{E_{X,p} + E_R E_{X,s}} \tag{27}$$

where the $E_{X,p}$ and $E_{X,s}$ are values of the specific exergy of primary inlet and secondary inlet.

The calculation result is displayed in Fig. 14. Among them, Fig. 14(a) indicates the change trend of the two under the change of primary inlet pressure. It can be seen that with the increase of pressure, s_{gen} and E_D tend to decrease first and then increase, which indicates that the available energy lost in the ejector due to irreversible process decreases first and then increases, the exergy destruction ratio (ξ_D) also decreased from 56.6% to 47.8%, and then increased to 48.6%. Because the greater the available energy loss leads to lower working efficiency, explaining the internal reason that the ejector performance increases first and then decreases with the increase of primary pressure. Similarly, with the increase of primary temperature (Fig. 14(b)), s_{gen} and E_D decrease. When the temperature is 313.7 K, the ξ_D can be reduced to 10.2%, and the energy loss caused by irreversible process decreases greatly, so the ejector performance will also be greatly improved. Finally, when the back pressure changes (Fig. 14(c)), due to the existence of critical back pressure, before the critical back pressure, the irreversible process caused by the double blocking state does not affect the internal s_{gen} and E_D. Once the critical back pressure is crossed, the two will rise rapidly with the increase of back pressure. When the back pressure is set at 4.0 MPa, the ξ_D is as high as 72.9%, and in this case, the ejector capacity will be quickly restricted. For greater clarity and visualization, the data are presented in Table 5.

For the sake of synthesis, this section also introduces a more practical

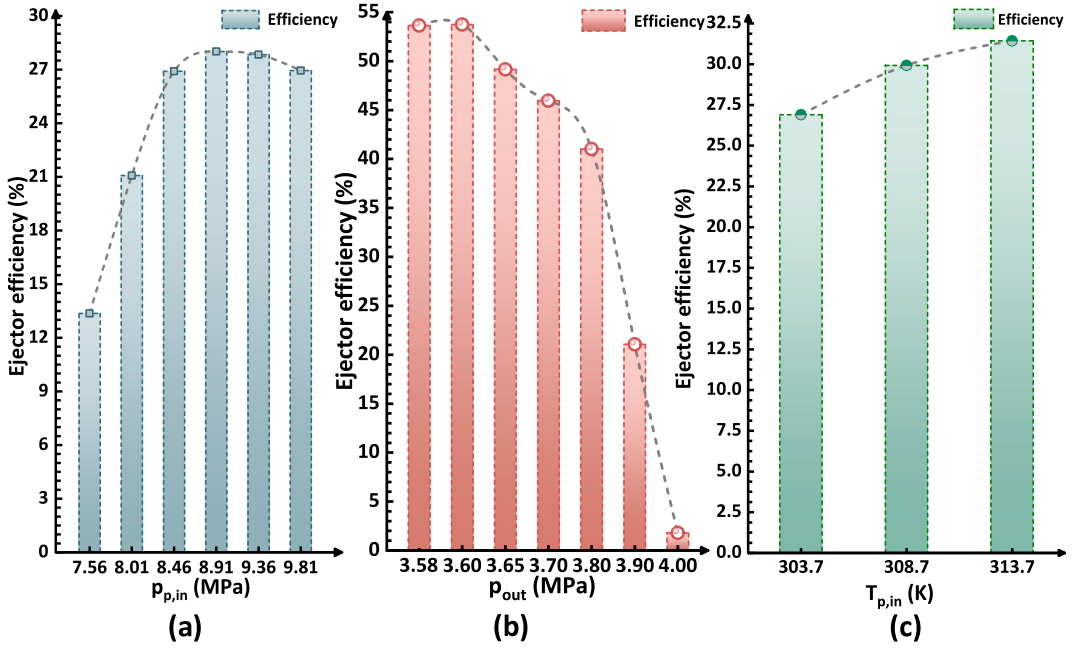

Fig. 15. Comparison of ejector efficiency under different operating conditions: (a) Under different primary inlet pressures; (b) Under different outlet pressures; (c) Under different primary inlet temperatures.

definition efficiency η, which is exploited to assess the merit or otherwise of the performance of the ejector. Its calculation can be expressed as follows.

$$\eta_{ej} = ER\frac{h\left(p_{diff,out}, s_{s,in}\right) - h_{s,in}}{h_{p,in} - h\left(p_{diff,out}, s_{p,in}\right)} \tag{28}$$

Here, h and s represent enthalpy and entropy respectively, which is consistent with the previous article. The subscripts diff,out, p,in and s,in are used to represent the diffuser outlet, the inlet of the primary flow and the secondary flow respectively, all of which are consistent with the above.

As shown in Fig. 15, consistent with irreversible energy loss under variable conditions, the overall efficiency of ejector is contrary to s_{gen} and E_D, but consistent with ejector entrainment performance. After calculation, when the $p_{p,in}$ is 8.01 MPa and the p_{out} is 3.58 MPa and 3.6 MPa, the efficiency reaches the maximum, which is about 54%. However, when the p_{out} is close to the backflow state of 4.0 MPa, the ejector efficiency drops rapidly to only 1.8%, which is no longer in normal working condition. According to Fig. 15, it can also be judged that in order to obtain higher injection efficiency, it is necessary to take into account multi-boundary conditions and reasonably select outlet pressure or temperature at different inlet pressures or temperatures, so as to ensure less energy loss and higher performance efficiency at lower operating costs.

5. Conclusions

A numerical model of two-phase CO_2 flow considering non-equilibrium phase change in ejector was established. The effectiveness and accuracy of the model were validated by the existing experimental data. Different operating conditions are taken as the entry point for analysis, and the influence of that on the characteristics of two-phase flow and entrainment performance in ejector was investigated. In particular, from the point of view of energy, the entropy generation and energy destruction in the ejector were discussed, and the working efficiency characteristics of the ejector were expounded by coupling mass transfer and energy change. The main conclusions are as follows:

1. As the primary inlet pressure continuously increases, the high-speed region inside the mixing chamber expands. Obvious shock wave will form at the outlet of ejector nozzle, which will cause the ejector performance to rise to a certain value and then decline.
2. With an increase in the primary inlet temperature, the gas volume fraction and mixing density increase, and the entrainment performance is improved. When the back pressure setting exceeds the critical back pressure, the entrainment performance drops rapidly and the ejector will not work normally.
3. It is calculated that intensive mass transfer behavior exists closing to the nozzle throat, and the position of mass transfer is advanced due to the increase of primary temperature. At the temperature of 313.7 K, the mass transfer rate at the throat can reach $7.69*10^7$ kg/m^3/s. However, the increase of back pressure leads to the mass transfer phenomenon of the main nozzle moving backward.
4. Under variable operating conditions, the trends in entropy generation and exergy destruction are consistent. As the primary inlet pressure increases, the exergy destruction initially decreases to 98.73 kJ/kg and then subsequently rises to 99.68 kJ/kg. The overall efficiency will increase from 13% to 28% and then decreases to 27%.
5. With the increase in inlet temperature, both entropy generation and exergy destruction demonstrate a linear downward trend, indicating a significant improvement in efficiency. As the temperature rises from 303.7 K to 313.7 K, the efficiency of the ejector increases from 27% to 31%.
6. Once the outlet pressure exceeds the critical back pressure and exergy destruction begin to increase. When the back pressure reaches 4.0 MPa, the exergy destruction rapidly escalates to 106 kJ/kg, and the ratio of exergy destruction surges to 72.9%, while the efficiency plummets to merely 1.8%.

To sum up, establishing a suitable model of transcritical CO_2 two-phase ejector is the key to study its internal flow mechanism, and the analysis of its energy evolution trend will also provide guidance for its design.

CRediT authorship contribution statement

Hongbing Ding: Writing – original draft, Funding acquisition, Formal analysis, Conceptualization. **Yuanyuan Dong:** Writing – review & editing, Validation, Methodology, Formal analysis, Conceptualization. **Yan Yang:** Writing – review & editing, Supervision, Methodology, Formal analysis, Conceptualization. **Chuang Wen:** Writing – review & editing, Supervision, Methodology, Formal analysis, Conceptualization.

Declaration of competing interest

The authors declare that they have no known competing financial interests or personal relationships that could have appeared to influence the work reported in this paper.

Data availability

Data will be made available on request.

Acknowledgements

This work is supported by National Natural Science Foundation of China under Grant 52276159 and 62073135, the National Key Research and Development Program of China under Grant 2023YFB3209304 and the Engineering and Physical Sciences Research Council [grant number EP/X027147/1].

References

[1] Gao E, Cui Q, Jing H, Zhang Z, Zhang X. A review of application status and replacement progress of refrigerants in the Chinese cold chain industry. Int J Refrig 2021;128:104–17.
[2] Birmpili T. Montreal protocol at 30: the governance structure, the evolution, and the Kigali amendment. Compt Rendus Geosci 2018;350:425–31.
[3] Bansal P. A review – status of CO2 as a low temperature refrigerant: fundamentals and R&D opportunities. Appl Therm Eng 2012;41:18–29.
[4] Bhattacharyya SS, Leite FFGD, Adeyemi MA, Sarker AJ, Cambareri GS, Faverin C, et al. A paradigm shift to CO2 sequestration to manage global warming – with the emphasis on developing countries. Sci Total Environ 2021;790:148169.
[5] Kasaeian A, Hosseini SM, Sheikhpour M, Mahian O, Yan W, Wongwises S. Applications of eco-friendly refrigerants and nanorefrigerants: a review. Renew Sust Energ Rev 2018;96:91–9.
[6] Al-Sayyab AKS, Mota-Babiloni A, Navarro-Esbrí J. Performance evaluation of modified compound organic Rankine-vapour compression cycle with two cooling levels, heating, and power generation. Appl Energ 2023;334:120651.
[7] Yu B, Long J, Zhang Y, Ouyang H, Wang D, Shi J, et al. Life cycle climate performance evaluation (LCCP) of electric vehicle heat pumps using low-GWP refrigerants towards China's carbon neutrality. Appl Energ 2024;353:122061.
[8] Wang W, Zhao Z, Zhou Q, Qiao Y, Cao F. Model predictive control for the operation of a transcritical CO2 air source heat pump water heater. Appl Energ 2021;300:117339.
[9] Gullo P, Hafner A, Banasiak K. Transcritical R744 refrigeration systems for supermarket applications: current status and future perspectives. Int J Refrig 2018;93:269–310.
[10] Jeon Y, Kim S, Lee SH, Chung HJ, Kim Y. Seasonal energy performance characteristics of novel ejector-expansion air conditioners with low-GWP refrigerants. Appl Energ 2020;278:115715.
[11] Yu B, Yang J, Wang D, Shi J, Chen J. An updated review of recent advances on modified technologies in transcritical CO2 refrigeration cycle. Energy (Oxford) 2019;189:116147.
[12] Elbel S, Lawrence N. Review of recent developments in advanced ejector technology. Int J Refrig 2016;62:1–18.

[13] Palacz M, Bodys J, Haida M, Smolka J, Nowak AJ. Two-phase flow visualisation in the R744 vapour ejector for refrigeration systems. Appl Therm Eng 2022;210:118322.
[14] Ding H, Dong Y, Zhang Y, Wen C, Yang Y. Exergy performance analysis of hydrogen recirculation ejectors exhibiting phase change behaviour in PEMFC applications. Energy 2024;300:131563.
[15] Chen Z, Zhao H, Kong F, Liu G, Wang L, Lai Y. Synergistic effect of adjustable ejector structure and operating parameters in solar-driven ejector refrigeration system. Sol Energy 2023;250:295–311.
[16] Tashtoush BM, Al-Nimr MA, Khasawneh MA. A comprehensive review of ejector design, performance, and applications. Appl Energ 2019;240:138–72.
[17] Ding H, Dong Y, Zhang Y, Yang Y, Wen C. Energy efficiency assessment of hydrogen recirculation ejectors for proton exchange membrane fuel cell (PEMFC) system. Appl Energ 2023;346:121357.
[18] Ringstad KE, Allouche Y, Gullo P, Ervik Å, Banasiak K, Hafner A. A detailed review on CO2 two-phase ejector flow modeling. Therm Sci Eng Prog 2020:20.
[19] Giacomelli F, Mazzelli F, Banasiak K, Hafner A, Milazzo A. Experimental and computational analysis of a R744 flashing ejector. Int J Refrig 2019;107:326–43.
[20] Zhu Y, Li C, Zhang F, Jiang P. Comprehensive experimental study on a transcritical CO2 ejector-expansion refrigeration system. Energ Convers Manage 2017;151:98–106.
[21] Banasiak K, Hafner A, Andresen T. Experimental and numerical investigation of the influence of the two-phase ejector geometry on the performance of the R744 heat pump. Int J Refrig 2012;35:1617–25.
[22] Lawrence N, Elbel S. Experimental investigation on control methods and strategies for off-design operation of the transcritical R744 two-phase ejector cycle. Int J Refrig 2019;106:570–82.
[23] Li Y, Deng J, Ma L, Zhang Y. Visualization of two-phase flow in primary nozzle of a transcritical CO2 ejector. Energ Convers Manage 2018;171:729–41.
[24] Li Y, Deng J, Ma L. Experimental study on the primary flow expansion characteristics in transcritical CO2 two-phase ejectors with different primary nozzle diverging angles. Energy (Oxford) 2019;186:115839.
[25] Zhu Y, Wang Z, Yang Y, Jiang P. Flow visualization of supersonic two-phase transcritical flow of CO2 in an ejector of a refrigeration system. Int J Refrig 2017;74:354–61.
[26] Haghparast P, Sorin MV, Nesreddine H. The impact of internal ejector working characteristics and geometry on the performance of a refrigeration cycle. Energy (Oxford) 2018;162:728–43.
[27] Zhu Y, Huang Y, Li C, Zhang F, Jiang P. Experimental investigation on the performance of transcritical CO2 ejector–expansion heat pump water heater system. Energ Convers Manage 2018;167:147–55.
[28] Liu G, Li H, Lu Z, Wang Y, Gong Y. Self-optimized efficient operation of trans-critical CO2 ejector-expansion heat pump water heater system with two-stage evaporation. Energ Build 2023;300:113659.
[29] Zhu J, Elbel S. Experimental investigation into the influence of vortex control on transcritical R744 ejector and cycle performance. Appl Therm Eng 2020;164:114418.
[30] Ge J, Chen H, Li J, Jin Y. Experimental comparison of critical performance for variable geometry ejectors with different mixer structures. Chem Eng J 2023;478:147487.
[31] Song Y, Ma Y, Wang H, Yin X, Cao F. Review on the simulation models of the two-phase-ejector used in the transcritical carbon dioxide systems. Int J Refrig 2020;119:434–47.
[32] Li F, Tian Q, Wu C, Wang X, Lee J. Ejector performance prediction at critical and subcritical operational modes. Appl Therm Eng 2017;115:444–54.
[33] Lucas C, Rusche H, Schroeder A, Koehler J. Numerical investigation of a two-phase CO2 ejector. Int J Refrig 2014;43:154–66.
[34] Haida M, Smolka J, Hafner A, Ostrowski Z, Palacz M, Nowak AJ, et al. System model derivation of the CO2 two-phase ejector based on the CFD-based reduced-order model. Energy (Oxford) 2018;144:941–56.
[35] Palacz M, Haida M, Smolka J, Nowak AJ, Banasiak K, Hafner A. HEM and HRM accuracy comparison for the simulation of CO2 expansion in two-phase ejectors for supermarket refrigeration systems. Appl Therm Eng 2017;115:160–9.
[36] Haida M, Smolka J, Hafner A, Palacz M, Banasiak K, Nowak AJ. Modified homogeneous relaxation model for the R744 trans-critical flow in a two-phase ejector. Int J Refrig 2018;85:314–33.
[37] Liao Y, Lucas D. Computational modelling of flash boiling flows: a literature survey. Int J Heat Mass Tran 2017;111:246–65.
[38] Liu F, Liu H, Liu Y, Yu G, Zhao X, Fan Y, et al. Transient numerical study of CO2 two-phase flow in a needle adjustable ejector. Int J Heat Mass Tran 2023;214:124395.
[39] Li Y, Deng J. Numerical investigation on the performance of transcritical CO2 two-phase ejector with a novel non-equilibrium CFD model. Energy (Oxford) 2022;238:121995.
[40] Yazdani M, Alahyari AA, Radcliff TD. Numerical modeling of two-phase supersonic ejectors for work-recovery applications. Int J Heat Mass Tran 2012;55:5744–53.
[41] Colarossi M, Trask N, Schmidt DP, Bergander MJ. Multidimensional modeling of condensing two-phase ejector flow. Int J Refrig 2012;35:290–9.
[42] Long J, Yu B, Wang D, Liu C, Shi J, Chen J. A novel relaxation drift model for simulating liquid-vapor momentum non-equilibrium in two-phase ejectors. Case Stud Therm Eng 2023;52:103758.
[43] Kumar Yadav V, Prakash Bijarniya J, Sarkar J, Ghosh P. Techno-economic assessment of solar-driven ejector refrigeration system assisted with daytime radiative condenser. Energ Convers Manage 2024;301:118051.
[44] Abed AM, Majdi SH, Sopian K, Ali FH, Al-Bahrani M, Al-Amir QR, et al. Techno-economic analysis of dual ejectors solar assisted combined absorption cooling cycle. Case Stud Therm Eng 2022;39:102423.
[45] Liu Z, Liu Z, Cao X, Li H, Yang X. Self-condensing transcritical CO2 cogeneration system with extraction turbine and ejector refrigeration cycle: a techno-economic assessment study. Energy (Oxford) 2020;208:118391.
[46] Habibi M, Aligolzadeh F, Hakkaki-Fard A. A techno-economic analysis of geothermal ejector cooling system. Energy (Oxford) 2020;193:116760.
[47] Banasiak K, Palacz M, Hafner A, Buliński Z, Smołka J, Nowak AJ, et al. A CFD-based investigation of the energy performance of two-phase R744 ejectors to recover the expansion work in refrigeration systems: an irreversibility analysis. Int J Refrig 2014;40:328–37.
[48] Smolka J, Bulinski Z, Fic A, Nowak AJ, Banasiak K, Hafner A. A computational model of a transcritical R744 ejector based on a homogeneous real fluid approach. Appl Math Model 2013;37:1208–24.
[49] Lakzian E, Yazdani S, Salmani F, Mahian O, Kim HD, Ghalambaz M, et al. Supersonic separation towards sustainable gas removal and carbon capture. Prog Energy Combust Sci 2024;103:101158.
[50] Haida M, Smolka J, Hafner A, Mastrowski M, Palacz M, Madsen KB, et al. Numerical investigation of heat transfer in a CO2 two-phase ejector. Energy (Oxford) 2018;163:682–98.
[51] Sauer J, Winkler G, Schnerr GH. Cavitation and condensation - common aspects of physical modeling and numerical approach. Chem Eng Technol 2000;23:663–6.
[52] Lee WH, Lyczkowski RW. The basic character of five two-phase flow model equation sets. Int J Numer Meth Fl 2000;33:1075–98.
[53] Brennen CE. Fundamentals of multiphase flow. Cambridge, UK;New York: Cambridge University Press; 2009.